Journal of Computational Physics **177,** 394–417 (2002)
doi:10.1006/jcph.2002.7013, available online at http://www.idealibrary.com on IDEAL®

The Time-Line Interpolation Method for Large-Time-Step Godunov-Type Schemes

Vincent Guinot[1]

International Institute for Infrastructural, Hydraulics, and Environmental Engineering—IHE, Westvest 7, P.O. Box 3015, 2601 DA Delft, The Netherlands
E-mail: vgt@ihe.nl

Received November 28, 2000; revised August 6, 2001

This paper describes the use of the time-line interpolation procedure for the design of large-time-step, Godunov-type schemes for systems of hyperbolic conservation laws in one dimension. These schemes are based on a specific procedure to characterize the left and right states of the Riemann problems at the cell interfaces when the Courant number associated with the waves exceeds unity. To do so, the time-line interpolation technique is used. Constant and linear reconstruction techniques are presented. Sonic or critical points are seen to be a source of difficulty in the algorithm and an appropriate treatment is proposed. The algorithms are applied to the linear advection equation, to the inviscid Burgers equation, and to the set of hyperbolic conservation laws that describe shallow water flow in one dimension. These simulations show the superiority of the linear time reconstruction over the use of a constant time reconstruction. When the linear reconstruction technique is used, the modulus of the amplification factor of the scheme is equal to unity for all wave numbers, inducing oscillations in the computed profile owing to the phase error. The introduction of a slope limiter allows these oscillations to be eliminated, but yields numerical diffusion, thus restricting the range of applications of the scheme.

Key Words: conservation laws; shocks and singularities; Riemann–Hilbert problems; Stokes and Navier–Stokes equations; other equations arising in fluid mechanics; stability and convergence of numerical methods; transonic flows; compressible fluids, general.

1. INTRODUCTION

Godunov-type schemes have proved to be powerful tools for simulating discontinuous flows when they are described by systems of nonlinear, hyperbolic conservation laws [1, 2].

[1] Fax: +31-(0)-15-212-2129.

0021-9991/02 $35.00

Although they have gained popularity in the research area, such schemes are rarely found in simulation packages available commercially. Besides historical reasons for this, such schemes use many *ad hoc* techniques, such as slope limiters or wave splitting for multidimensional problems, and induce many spurious, undesirable effects on the computed solutions (see, e.g., [3–5]), making it difficult to solve problems where both strong shocks and acoustic wave are present. Also, because the stencil of a scheme should include the domain of dependence of the solution for stability, a Courant–Friedrichs–Lewy (CFL) stability constraint is necessarily attached to *fixed-stencil* schemes. Therefore, in such schemes, the computational time step has to be limited so the Courant number associated with each of the eigenvalues of the hyperbolic system should often be smaller than a fixed value. Consequently, such schemes fail to attain optimal efficiency when (i) large contrasts exist between the various eigenvalues, and (ii) the computational grid is highly irregular. In such cases, the scheme performance is limited by the largest of the eigenvalues of the hyperbolic system and by the size of the smallest cell, leading to a strong degradation of the numerical solution in regions where the grid is larger.

Efforts made in the past to overcome stability problems have led to a first class of numerical methods where the governing partial differential equations (PDEs) are approximated with ordinary differential equations (ODEs), thus breaking the dependence of the time step on the cell size [6–9]. Although this allows the computational time step to be increased, such an approach has the drawback that it only works for smooth solutions to the PDEs.

Another possible approach consists of adapting the stencil of the scheme to the size of the domain of dependence of the solution. The characteristics can be traced forward or backward across several computational cells. This has been the subject of various works in the domain of Lagrangian or semi-Lagrangian techniques [10, 11] as well as flux-based (or conservative) Eulerian schemes [12–15]. Originally, the approach consisted of seeking the departure point of the characteristic lines across several cells when needed. It was applied to problems with (almost) constant wave speeds (such as water hammer problems [10]), because it is very easy to locate the feet of the characteristic lines in such a case. The accurate determination of the feet of the characteristic lines is not straightforward and has been studied by a number of authors (see, e.g., [16, 17]). Moreover, when strong nonlinearities are present in the equations, the irreversible character of the solution makes it difficult, if not impossible, to determine accurately the extension of the domain of dependence using backward-tracking algorithms.

A third approach, well suited to the solution of conservation laws in the presence of shock waves, consists of using front-tracking-based methods [18–20], except that the domain of influence and the potential merging of shocks is explored *forward* in time rather than backward.

The fourth approach consists of making the scheme implicit by solving a set of linear or nonlinear equations using the unknown variables at the next time level to be computed [21–24]. These techniques are time consuming, inasmuch as the size of the system to be solved is equal to the number of computational cells, or to twice this number in some methods.

The technique proposed in the present paper is based on a fixed, three-cell stencil, that is, the minimum size for a finite-volume-based scheme for hyperbolic problems with positive and negative wave speeds. It uses the equivalence between time and space (which is a characteristic of hyperbolic systems) to deal with the increase in the size of the domain of dependence of the solution. It involves the solution of a set of recurrence relationships on the left and right states of the Riemann problems at the cell interfaces, but these relationships

can be solved in a single sweep for each state, which makes the proposed scheme as cheap as a classical, fixed-stencil explicit scheme. Typical applications of this scheme are for problems where the fastest waves in the solution do not need to be resolved as accurately as the slowest ones (typical application: solute or sediment transport in rivers, where the modeler is interested in a good resolution of the sediment profile and does not need a refined solution of the hydrodynamics) or where the grid is subject to local refinement in a few points owing to geometrical constraints, but where it is more important to have a good resolution of the solution in the parts of the domain where the grid size is larger (typical application: single- or two-phase flow in pipe networks, where local refinements of the mesh are needed in order to describe valves, diaphragms, etc.). The method is presented for one-dimensional conservation laws. It could easily be extended to multidimensional problems via alternate directions or wave splitting (see, e.g., [20] for a description of the wave-splitting approach), but it is believed that these methods are not fully satisfactory for multidimensional problems, in particular when large time steps are involved. The design of genuinely multidimensional schemes based on the proposed time-line interpolation approach is under investigation at the moment.

Section 2 presents the principle of the time-line reconstruction technique for systems of conservation laws. Section 3 deals with the particular problem of sonic points (also called critical points in hydraulic applications), which have been identified to need a specific treatment. Computational examples are presented in Section 4 and Section 5 is devoted to concluding remarks. Appendix A details the derivation of the linear time reconstruction and Appendix B is devoted to its linear stability analysis.

2. TIME-LINE INTERPOLATION

2.1. Principle

The time-line interpolation technique is based on the equivalence between space and time that is the feature of hyperbolic systems of conservation laws. Such systems can be written in one dimension in conservative form.

$$\frac{\partial \mathbf{U}}{\partial t} + \frac{\partial \mathbf{F}}{\partial x} = 0, \tag{1}$$

where $\mathbf{U}$ is the conserved variable, $\mathbf{F}$ is the flux function dependent on $\mathbf{U}$, t is time, and x is the space coordinate. $\mathbf{U}$ and $\mathbf{F}$ are vectors of size m. Another alternative to Eq. (1) is the nonconservative form,

$$\frac{\partial \mathbf{U}}{\partial t} + \mathbf{A}\frac{\partial \mathbf{U}}{\partial x} = 0, \tag{2}$$

where $\mathbf{A}$ is the Jacobian matrix of $\mathbf{F}$ with respect to $\mathbf{U}$. The system is said to be an $m \times m$ hyperbolic system if the matrix $\mathbf{A}$ has m real eigenvalues. The present paper focuses on discretizations of Eq. (1) in the form

$$\mathbf{U}_j^{n+1} = \mathbf{U}_j^n + \frac{\Delta t}{\Delta x_j}\left(\bar{\mathbf{F}}_{j-1/2} - \bar{\mathbf{F}}_{j+1/2}\right), \tag{3}$$

where $\mathbf{U}_j^n$ denotes the average value of $\mathbf{U}$ over cell j at time level n, and $\bar{\mathbf{F}}_{j+1/2}$ represents the average of the flux $\mathbf{F}$ at the interface between cells j and $j+1$ between time levels n and

$n+1$. Δx_j is the width of cell j and Δt is the computational time step. In Godunov-type algorithms, the flux $\bar{\mathbf{F}}_{j+1/2}$ is computed directly using the average value of $\mathbf{U}$.

$$\bar{\mathbf{F}}_{j+1/2} = \mathbf{F}\big(\bar{\mathbf{U}}_{j+1/2}\big), \tag{4}$$

where $\bar{\mathbf{U}}_{j+1/2}$ is the solution to the Riemann problem:

$$\mathbf{U}(x, t^n) = \mathbf{U}_{j+1/2,L}, x \le x_{j+1/2}, \tag{5a}$$

$$\mathbf{U}(x, t^n) = \mathbf{U}_{j+1/2,R}, x > x_{j+1/2}. \tag{5b}$$

The Riemann problem is solved using exact or approximate solvers and the value of the variable at the interface is used to compute the flux. Except in very simple cases, such as linear laws, the solution of the Riemann problem can be found only for piecewise constant initial data. In this case, the flux at the location of the initial discontinuity is independent of time. Therefore, it is convenient to transform a nonconstant reconstructed variable into a classical Riemann problem, because many exact and approximate solvers can be used for this. In higher-order schemes, the left and right states of the Riemann problem are obtained by a particular averaging of the variable $\mathbf{U}$ over the domain of dependence of the characteristics [2, 25–27]. This averaging is also called the generalized Riemann problem (GRP) method. Note that the averaging of the variable on each side of the interface may result in a discontinuous Riemann problem, even though the reconstructed profile is continuous across the interface. This is because the solution at the interface over one time step is influenced not only by the initial value of the variable at the interface but by all the values of the variable within the domain of influence of the solution. This is observed for instance in the PPM scheme [27], where the parabolic reconstructed profiles, although joining each other at the cell interfaces, result in piecewise constant data. The class of schemes presented in what follows also uses the GRP approach. The present contribution focuses on determining the left and right states $\mathbf{U}_{j+1/2,L}$ and $\mathbf{U}_{j+1/2,R}$ of the Riemann problem when the Courant number is larger than unity.

Consider first that the flow is continuous between time levels n and $n+1$ in cells j and $j+1$. This is not necessarily true in all situations, but practical implementations show [3, 4, 28] that the following analysis, which is valid only in the case of a continuous solution, does not introduce too strong a bias, even in the presence of discontinuities. Under the assumption of smooth flow, $\bar{\mathbf{U}}_{j+1/2}$ is given by

$$\bar{\mathbf{U}}_{j+1/2} = \frac{1}{\Delta t} \int_{t^n}^{t^{n+1}} \mathbf{U}_{j+1/2}(t)\, dt. \tag{6}$$

$\mathbf{U}$ can also be expressed as a linear combination of the eigenvectors of $\mathbf{A}$.

$$\mathbf{U} = \sum_p \alpha^{(p)} \mathbf{K}^{(p)}, \tag{7}$$

where $\mathbf{K}^{(p)}$ is the pth eigenvector of $\mathbf{A}$ and $\alpha^{(p)}$ is the corresponding wave strength.

Substituting Eq. (7) into Eq. (6) yields

$$\bar{\mathbf{U}}_{j+1/2} = \sum_p \frac{1}{\Delta t} \int_{t^n}^{t^{n+1}} \alpha^{(p)} \mathbf{K}^{(p)}_{j+1/2}(t)\, dt. \tag{8}$$

Separating positive from negative eigenvalues, Eq. (8) can also be rewritten as

$$\bar{\mathbf{U}}_{j+1/2} = \sum_{p,\lambda^{(p)}\geq 0} \frac{1}{\Delta t} \int_{t^n}^{t^{n+1}} \alpha^{(p)} \mathbf{K}^{(p)}_{j}(t)\, dt + \sum_{q,\lambda^{(q)}<0} \frac{1}{\Delta t} \int_{t^n}^{t^{n+1}} \alpha^{(q)} \mathbf{K}^{(q)}_{j+1}(t)\, dt. \tag{9}$$

Since this solution has to be obtained through the solution of an equivalent Riemann problem, the following relationship must also hold:

$$\bar{\mathbf{U}}_{j+1/2} = \sum_{p,\lambda^{(p)}\geq 0} \frac{1}{\Delta t} \int_{t^n}^{t^{n+1}} \alpha^{(p)} \mathbf{K}^{(p)}_{j+1/2,L}(t)\, dt + \sum_{q,\lambda^{(q)}<0} \frac{1}{\Delta t} \int_{t^n}^{t^{n+1}} \alpha^{(q)} \mathbf{K}^{(q)}_{j+1/2,R}(t)\, dt. \tag{10}$$

The consequence is a condition on the left and right states of the equivalent Riemann problem. The left state has to be defined in such a way that the wave strengths associated with the positive eigenvalues of the equivalent problem are the same as those obtained from the real variable. It should be noticed that the wave strengths associated with the negative eigenvalues can be chosen arbitrarily. Conversely, the right state of the equivalent Riemann problem has to be defined such that the wave strengths associated with the negative eigenvalues are the same as those obtained from the real variable.

Consider now the pth wave and assume the pth eigenvalue is positive. The average of the pth component of the wave can be computed using the theory of characteristics, which states that the following relationship holds.

$$d\mathbf{K}^{(p)} = 0 \text{ along } \frac{dx}{dt} = \lambda^{(p)}, \tag{11}$$

where $\lambda^{(p)}$ is the pth eigenvalue of $\mathbf{A}$. The classical GRP approach makes use of Eq. (11) to convert the average of $\mathbf{K}^{(p)}$ over time into its average over the domain of dependence of the pth characteristic.

$$\frac{1}{\Delta t} \int_{t^n}^{t^{n+1}} \alpha(p)^n \mathbf{K}^{(p)}_{j+1/2}(t)\, dt = \frac{1}{x_{j+1/2} - x_A} \int_{x_A}^{x_{j+1/2}} \alpha(p)^n \mathbf{K}^{(p)^n}(x)\, dx, \tag{12}$$

where A is the foot of the pth characteristic originating from the interface at time level $n+1$ and x_A is its abscissa.

The initial distribution $\alpha^{(p)^n}\mathbf{K}^{(p)^n}(x)$ is computed from the reconstructed profile $\mathbf{U}^n(x)$ of the conserved variable. When the Courant number, defined by

$$Cr = \max_p \left(\left|\lambda^{(p)}\right|_{\lambda^{(p)}\geq 0} \frac{\Delta t}{\Delta x_j}, \left|\lambda^{(p)}\right|_{\lambda^{(p)}<0} \frac{\Delta t}{\Delta x_{j+1}} \right), \tag{13}$$

is smaller than unity, the spatial average in Eq. (12) is straightforward to compute because the foot of the characteristic lies either within cell j or within cell $j+1$. For the left-hand side of the interface $j+1/2$, all wave strengths for the positive eigenvalues can be computed in a similar way. The wave strengths associated with the negative eigenvalues can be assigned any arbitrary value, because they will not influence the solution of the Riemann problem, as stated above. The simplest solution is to compute them from the average $\mathbf{U}_j^n$ over the cell.

On the other hand, if the Courant number is larger than 1, the foot of the characteristic must be sought in the cells located to the left of cell j (for a positive wave speed) or to the right of cell $j+1$ (for a negative wave speed). Then, owing to the possible presence of shocks in the solution (which may arise from the Riemann problem at interface $j-1/2$ or $j+3/2$), backtracking of the characteristic becomes an ill-posed problem. This is due to the irreversible character of the shock propagation process, where different initial conditions may lead to the same final state. Therefore, backward tracking of the characteristic is not used in the proposed approach. Instead, when a characteristic crosses a cell interface, it is better to use the information available over time at this interface. Equation (12) is then separated into

$$\frac{1}{\Delta t}\int_{t^n}^{t^{n+1}} \alpha_{j+1/2}^{(p)}\mathbf{K}_{j+1/2}^{(p)}(t)\,dt = \frac{1}{\Delta t}\int_{t^n}^{\tau} \alpha_{j+1/2}^{(p)}\mathbf{K}_{j+1/2}^{(p)}(t)\,dt + \frac{1}{\Delta t}\int_{\tau}^{t^{n+1}} \alpha_{j+1/2}^{(p)}\mathbf{K}_{j+1/2}^{(p)}(t)\,dt, \quad (14)$$

where τ is the time at which the pth characteristic, which originated from the neighboring interface (either $j-1/2$ or $j+3/2$) at time level n, crosses the interface $j+1/2$ (illustrated in Fig. 1 for positive $\lambda^{(p)}$).

Assuming that $\lambda^{(p)}$ is positive, the two terms on the right-hand side of Eq. (14) are computed as follows.

$$\frac{1}{\tau - t^n}\int_{t^n}^{\tau} \alpha_{j+1/2}^{(p)}\mathbf{K}_{j+1/2}^{(p)}(t)\,dt = \frac{1}{\Delta x_j}\int_{x_{j-1/2}}^{x_{j+1/2}} \alpha^{(p)}\mathbf{K}^{(p)^n}(x)\,dx = \alpha_j^{(p)}\mathbf{K}_j^{(p)^n}, \quad (15a)$$

$$\int_{\tau}^{t^{n+1}} \alpha_{j+1/2}^{(p)}\mathbf{K}_{j+1/2}^{(p)}(t)\,dt = \frac{t^{n+1}-\tau}{\tau' - t^n}\int_{t^n}^{\tau'} \alpha_{j-1/2}^{(p)}\mathbf{K}_{j-1/2}^{(p)}(t)\,dt, \quad (15b)$$

where τ' is the time at which the characteristic, originating from $j+1/2$ at time level $n+1$, intersects the interface $j-1/2$. Since backward tracking is not used, τ and τ' are

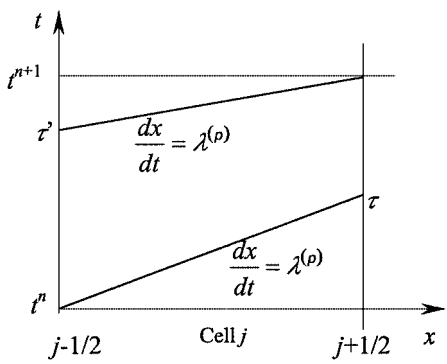

FIG. 1. Use of time reconstruction.

not determined using the value of $\lambda^{(p)}$ in cell j only. The preferred formula is

$$\tau = t^n + \frac{\Delta x_j}{\mathrm{Max}\left(\bar{\lambda}^{(p)}_{j-1/2}, \lambda^{(p)^n_j}\right)}, \tag{16a}$$

$$\tau' = t^{n+1} - \frac{\Delta x_j}{\bar{\lambda}^{(p)}_{j-1/2}}, \tag{16b}$$

where $\lambda^{(p)^n_j}$ is computed using $\mathbf{U}^n_j$, and $\bar{\lambda}^{(p)}_{j-1/2}$ is the wave speed computed from the average value $\bar{\mathbf{U}}_{j-1/2}$. Equation (16a) uses the maximum of the eigenvalues to reinforce the upwind character of the scheme: if the pth wave is a shock, its speed is necessary between the two values $\lambda^{(p)^n_j}$ and $\bar{\lambda}^{(p)}{}_{j-1/2}$. Taking the maximum of the two adds extra diffusion and allows possible oscillations arising from the shock to be dissipated. This is an essential feature of the scheme that precludes very efficiently nonlinear instabilities from occurring. Since the negative components of the wave do not have any influence on the solution, they can be taken equal to those of $\mathbf{U}^n_j$. The set of equations (14)–(16) can be used as recurrence relationships for the definition of the components associated with the positive eigenvalues. Therefore, a single sweep from the left to the right allows the left states of the Riemann problems to be defined, whereas a single sweep from the right to the left allows the right states of the Riemann problems to be fully determined. The proposed approach is no more computationally expensive than a classical explicit method.

2.2. Constant Time Reconstruction

The key feature of the scheme is the way in which the quantity $\alpha^{(p)}_{j-1/2}\mathbf{K}^{(p)}_{j-1/2}(t)$ is reconstructed in time. The schemes presented here use either a constant or a linear reconstruction. For the sake of clarity, the quantity $\alpha^{(p)}_{j-1/2}\mathbf{K}^{(p)}_{j-1/2}(t)$ is denoted hereafter by $\phi(t)$ and the recurrence relationship is given for positive eigenvalues only, i.e., for the left-hand side of the Riemann problem. Equation (14) becomes

$$\bar{\phi}_{j+1/2,L} = \frac{1}{\Delta t}\int_{t^n}^{t^{n+1}} \phi_{j+1/2,L}(t)\,dt = \frac{1}{\Delta t}\int_{t^n}^{\tau} \phi_{j+1/2,L}(t)\,dt + \frac{1}{\Delta t}\int_{\tau}^{t^{n+1}} \phi_{j+1/2,L}(t)\,dt. \tag{17}$$

When the constant reconstruction in time is adopted, the two terms on the right-hand side of Eq. (17) are given by

$$\frac{1}{\Delta t}\int_{t^n}^{\tau} \phi_{j+1/2,L}(t)\,dt = \frac{1}{Cr}\phi^n_j, \tag{18a}$$

$$\frac{1}{\Delta t}\int_{\tau}^{t^{n+1}} \phi_{j-1/2,L}(t)\,dt = \frac{t^{n+1}-\tau}{\Delta t}\bar{\phi}_{j-1/2,L}. \tag{18b}$$

Substituting Eq. (18) into Eq. (17) yields

$$\bar{\phi}_{j+1/2,L} = \frac{1}{Cr}\phi^n_j + \left(1 - \frac{1}{Cr}\right)\bar{\phi}_{j-1/2,L}, \tag{19a}$$

$$Cr = \frac{\Delta t}{\tau - t^n}. \tag{19b}$$

2.3. Linear Time-Line Reconstruction

When the linear reconstruction in time is chosen, the profile is sought in the form

$$\phi_{j-1/2,L}(t) = \bar{\phi}_{j-1/2,L} + \left(t - t^n - \frac{\Delta t}{2}\right) s_{j-1/2,L}, \tag{20}$$

where $s_{j-1/2}$ is the (constant) "slope" over time of the variable at the interface $j - 1/2$. It is easy to check (see Appendix A) that the following recurrence relationships hold:

$$\bar{\phi}_{j+1/2,L} = \frac{\phi_j^n}{Cr} + \left(1 - \frac{1}{Cr}\right)\left(\bar{\phi}_{j-1/2,L} - \frac{\Delta t}{2Cr} s_{j-1/2,L}\right), \tag{21a}$$

$$s_{j+1/2,L} = -\frac{2}{\Delta t}\phi_j^n + \frac{2}{\Delta t}\bar{\phi}_{j-1/2,L} - \frac{1}{Cr} s_{j-1/2,L}. \tag{21b}$$

This version of the scheme is non-TVD and therefore has the drawback that oscillations may appear near steep fronts, which are a possible source for nonlinear instability. Consequently, s must be limited. Two slopes are computed,

$$\sigma_1 = 2\frac{\bar{\phi}_{j+1/2,L} - \phi_j^n}{\Delta t}, \tag{22a}$$

$$\sigma_2 = 2\frac{\bar{\phi}_{j-1/2,L} + \Delta t\left(\frac{1}{2} - \frac{1}{2Cr}\right) s_{j-1/2,L} - \bar{\phi}_{j+1/2,L}}{\Delta t}, \tag{22b}$$

and $s_{j+1/2}$ is corrected as follows:

$$s_{j+1/2,L} = \sigma_1 \quad \text{if } \sigma_1 s_{j+1/2,L} \geq 0 \text{ and } |\sigma_1| < s_{j+1/2,L}, \tag{23a}$$

$$s_{j+1/2,L} = \sigma_2 \quad \text{if } \sigma_2 s_{j+1/2,L} \geq 0 \text{ and } |\sigma_2| < s_{j+1/2,L}, \tag{23b}$$

$$s_{j+1/2,L} = 0 \quad \text{if } \sigma_1\sigma_2 \leq 0. \tag{23c}$$

A similar operation must be carried out for the right states of the Riemann problem. To do so, the mesh is swept from right to left.

3. TREATMENT OF SONIC/CRITICAL POINTS

Numerical experiments have shown that sonic (or critical) points (i.e., points at which a rarefaction wave exists and where one of the eigenvalues $\lambda^{(p)}$ switches from negative to positive values when going from left to right) may produce oscillations. This is due to the local change in the direction of propagation of the characteristic. In such a case, the dependence between the interface at which the sonic point is located and the next interface is broken. If the standard relationships (19) or (21)–(23) are used, this independence is not guaranteed. To ensure this independence, the following procedure is adopted.

Assume that there is a sonic point at interface $j - 1/2$, as illustrated in Fig. 2. The time at which the rarefaction wave hits the interface $j + 1/2$ is denoted by t_0. For times smaller than t_0, Eq. (18a) can still be used. But Eq. (18b) cannot be applied for further times, because in this equation the value of ϕ at $j + 1/2$ is a function of ϕ at $j - 1/2$, whereas this is not what happens in reality owing to the presence of the sonic point. The following procedure is adopted instead.

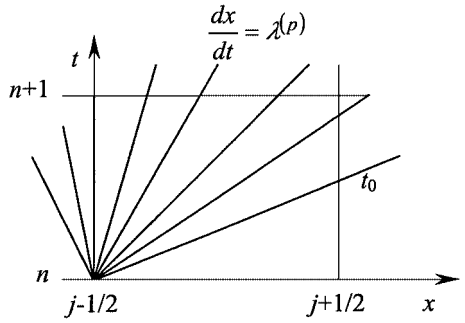

FIG. 2. Presence of a sonic point at interface $j - 1/2$.

The values $\bar{\mathbf{U}}_{j-1/2,L}$ and $\bar{\mathbf{U}}_{j-1/2,R}$ are recomputed so as to satisfy the relationships

$$\bar{\mathbf{U}}_{j-1/2,L} = \bar{\mathbf{U}}_{j-1/2,R} = \mathbf{U}, \tag{24a}$$

$$\lambda^{(p)}(\mathbf{U}) = 0, \tag{24b}$$

$$s^{(p)} = 0, \tag{24c}$$

where $\lambda^{(p)}(\mathbf{U})$ is the value of $\lambda^{(p)}$ computed using $\mathbf{U}$. $\mathbf{U}$ is obtained by solving the relationships

$$\frac{du_1}{k_1^{(p)}} = \frac{du_2}{k_2^{(p)}} = \cdots = \frac{du_m}{k_m^{(p)}}, \tag{25a}$$

$$\lambda^{(p)}(\mathbf{U}) = 0, \tag{25b}$$

where the quantity u_q is the qth component of vector $\mathbf{U}$ and $k_q^{(p)}$ is the qth component of the eigenvector $\mathbf{K}^{(p)}$. The relationships (25a) are valid across the pth wave, which connects $\mathbf{U}_{j-1}^n$ and $\mathbf{U}_j^n$ [29]. There are $m - 1$ such relationships that define $m - 1$ so-called "generalized Riemann invariants." The last relationship is provided by Eq. (25b). The number of equations is m for m unknows; therefore the solution $\mathbf{U}$ is unique in the general case.

4. BOUNDARY CONDITIONS

The recurrence relationships (14) on the left and right states of the Riemann problems at the cell interfaces can be written in the form

$$\overline{\alpha^{(p)} K_{j+1/2}^{(p)}} = g_{L,j+1/2}^{(p)} \left[\overline{\alpha^{(p)} K_{j-1/2}^{(p)}}\right] \quad \text{for } \lambda^{(p)} > 0, \tag{26a}$$

$$\overline{\alpha^{(p)} K_{j+1/2}^{(p)}} = g_{R,j+1/2}^{(p)} \left[\overline{\alpha^{(p)} K_{j+3/2}^{(p)}}\right] \quad \text{for } \lambda^{(p)} \leq 0. \tag{26b}$$

There are $N - m_L - m_R$ such conditions, where N is the number of cells in the computational domain, m_L is the number of positive eigenvalues at the left-hand boundary, and m_R is the number of negative eigenvalues at the right-hand boundary. For the solution to be unique, m_L conditions must be prescribed at the left-hand boundary and m_R conditions

have to be specified at the right-hand boundary. Such relationships can be written in the form

$$f_L^{(q)}\left[\bar{\mathbf{U}}_{1/2}^{(p)}\right] = 0, \tag{27a}$$

$$f_R^{(q)}\left[\bar{\mathbf{U}}_{N+1/2}^{(p)}\right] = 0, \tag{27b}$$

where $f_L^{(q)}$ and $f_R^{(q)}$ are known functions of the components $\mathbf{U}^{(p)}$. These relationships can be rewritten as functions of the wave strengths and of the eigenvectors:

$$f_R^{(q)}\left[\overline{\alpha^{(p)}\mathbf{K}^{(p)}}_{N+1/2}\right] = 0, \tag{28a}$$

$$f_L^{(q)}\left[\overline{\alpha^{(p)}\mathbf{K}^{(p)}}_{1/2}\right] = 0. \tag{28b}$$

Equations (26) and (28) form a $2mN \times 2mN$ system of nonlinear equations. A classical way of solving this system consists of starting with an arbitrary initial value for $\mathbf{U}$ at the left-hand boundary and to perform a forward sweep from interfaces $1/2$ to $N + 1/2$ using Eq. (26a). Then, Eq. (28b) provides the starting point for a backward sweep from the right-hand boundary to interface $1/2$ using Eq. (26b). Equation (28a) is used at the interface $1/2$ to update the value of $\mathbf{U}$ at the left-hand boundary. The forward and backward sweeps are repeated until satisfactory convergence is achieved. Depending on situations, this iterative procedure may be extremely time consuming and the proposed schemes may not necessarily be faster than classical implicit, iterative schemes. However, in most cases, it is not necessary to perform iterations, as shown by the following analysis for the constant time reconstruction and for a homogeneous Courant number.

Denoting again $\overline{\alpha^{(p)}\mathbf{K}^{(p)}}_{j-1/2}$ by $\bar{\phi}_{j-1/2}$ and assuming that the pth eigenvalue is positive, applying k times the constant time reconstruction between interfaces $1/2$ and $k + 1/2$ leads to a relationship of the type

$$\bar{\phi}_{1/2+k} = \sum_{r=1}^{k} a_{k,r}\phi_k^n + b_k\bar{\phi}_{1/2}. \tag{29}$$

Substituting Eq. (29) into Eq. (19a) yields, after straightforward algebra, the following condition on the coefficients b_k:

$$b_k = (1 - 1/Cr)^k. \tag{30}$$

Consequently, the influence of the value of the variable at the left-hand boundary on the value of variable at the right-hand boundary decreases exponentially with the number of points in the computational domain. An optimal number s_0 of forward and backward sweeps can thus be defined as

$$(1 - 1/Cr)^{2Ns_0} \leq \varepsilon, \tag{31}$$

where ε is a tolerance criterion defined by the user. The reason for the exponent $2Ns_0$ is that each forward sweep followed by a backward sweep involves $2N$ successive applications of the recurrence relationship from interface to interface. For example, for a Courant number of 10, one forward sweep followed by one backward sweep on a domain of 100 cells would

satisfy a tolerance criterion $\varepsilon = 10^{-9}$, whereas in practice, $\varepsilon = 10^{-3}$ or 10^{-2} proves to be sufficient. Equation (31) is also valid for the linear time reconstruction (which is less diffusive than the constant time reconstruction, even when the slope limiter is applied).

5. COMPUTATIONAL EXAMPLES

5.1. Scalar Linear Equation

The method was applied to the solution of the scalar advection equation:

$$\frac{\partial \phi}{\partial t} + \frac{\partial}{\partial x}(a\phi) = 0. \tag{32}$$

Three schemes were used: the constant time-line reconstruction, the linear without a limiter, and the linear with a limiter. The speed a was taken to be constant and the initial profile was a square shape. It was discretised using 20 cells. Figure 3 shows the computational results obtained using the three schemes after 20 time steps at a Courant number of 5.5. The classical first-order implicit upwind scheme was added for comparison. Since the method is finite-volume based, the quantities represented in Fig. 3 are the average values of the analytical and computed variables over the computational cells. While such averages are classically represented by point values at the center of the computational cells, they are represented using histograms, where the variable is constant and equal to the mean value over a given cell—hence the discontinuous aspect of the curves. This type of representation is preferred because the proposed numerical technique deals with average quantities over the computational cells. Note that this choice for a constant variable reconstruction within the cells is just as arbitrary as that of point values, since nothing can be said about the variable profile within the cells, unless a specific space reconstruction has been carried out. However, this way of presenting the computational results allows small oscillations in the profiles to be detected more easily than when the classical point representation is used. The constant time reconstruction already brings an improvement over the implicit, first-order upwind scheme. The linear time reconstruction leads to even better results when the limiter is used. If the limitation step is skipped, spurious oscillations appear in the computed profile, as shown by the dashed line with triangular dots in Fig. 3. Since the modulus of the amplification factor of the scheme is equal to unity when no limiter is used, these oscillations will never be damped. All calculations in what follows were carried out using the limiter.

It must be acknowledged however that neither the constant nor the linear time-line interpolation can achieve the accuracy of Lagrangian or flux-based Eulerian methods based on adaptive stencils [13–15, 18, 19]. The reason is that adaptive-stencil methods carry out only one profile interpolation (with or without slope limitation) at every time step to determine the flux across a given cell interface, whereas the spurious dissipation introduced by the constant time reconstruction or by the slope limiter of the proposed method is propagated within the same time level from one interface to the next via the recurrence relationships. Moreover, it should be stated that the adaptive stencil-based methods mentioned above provide the exact solution for integral values of the Courant number, and that their performance depends only on the fractional value of the Courant number (because the error due to variable interpolation occurs only in the cell that contains the foot of the characteristic issued from the interface).

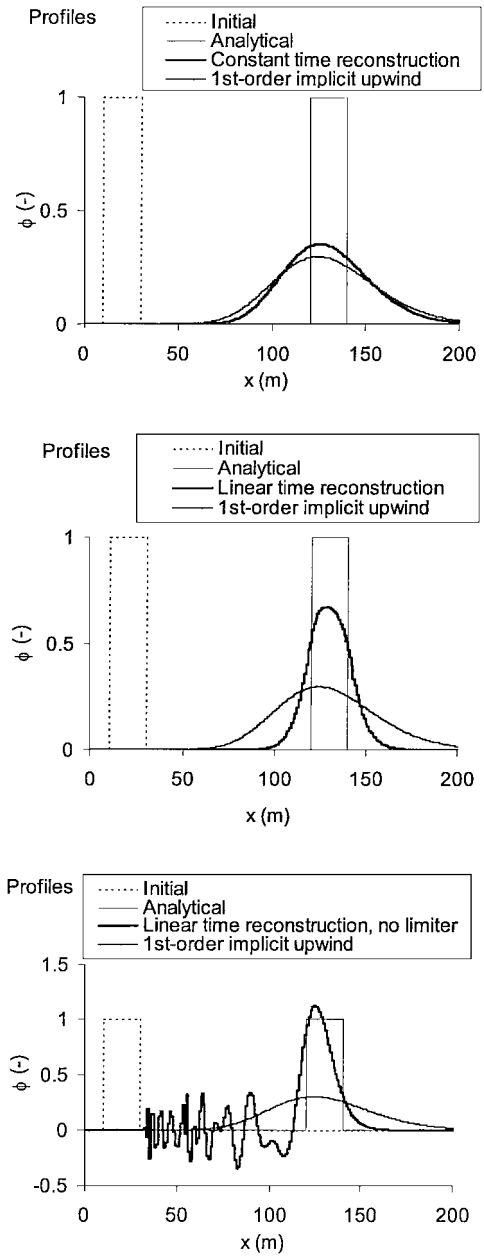

FIG. 3. Linear advection of a square profile after 20 time steps with a Courant number of 5.5.

5.2. Inviscid Burgers Equation

The constant and linear time reconstructions were applied to the inviscid Burgers equation:

$$\frac{\partial \phi}{\partial t} + \frac{\partial}{\partial x}\left(\frac{u^2}{2}\right) = 0. \tag{33}$$

The initial profile was a square. It was discretized using 20 cells of width 1. The base value of the profile was $\phi = 1$ and the top value was $\phi = 5$. The analytical solution consists of a

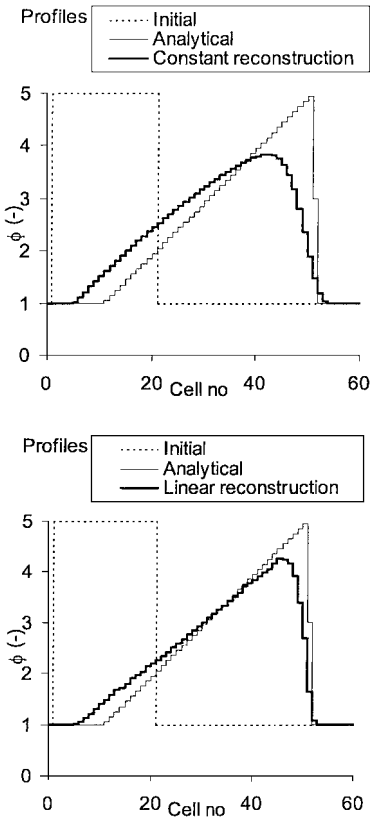

FIG. 4. Solution of the inviscid Burgers equation after 10 time steps with a maximum Courant number of 5.

shock and a rarefaction wave traveling to the right. The speed of the shock is initially 3. The head of the rarefaction wave travels at a speed of 5, whereas the tail travels at 1. Therefore, at $t = 10$, the rarefaction wave catches up with the shock. The analytical profile is then triangular. The time step was taken equal to 1; therefore the minimum and the maximum Courant numbers were 1 and 5, respectively. Figure 4 shows the computed profiles using the constant and linear time reconstructions at this time, together with the initial profile and the analytical solution.

Note that better profiles were obtained by modifying Eq. (16a) for the computation of τ. The formula

$$\tau = t^n + 2\frac{\Delta x_j}{\bar{\lambda}^{(p)}_{j-1/2} + \lambda^{(p)^n}_j} \tag{34}$$

allows fronts and tails of rarefaction waves to be located in a more accurate way. Equation (34) makes the implicit assumption that all waves can be treated as shocks, even though such an assumption violates the entropy condition for rarefaction waves. Nevertheless, experience shows that this assumption does not lead to any artificial sharpening of rarefaction waves and that Eq. (34) can be used safely. However, this modification gives good results only for the inviscid Burgers equation and cannot be recommended in the general case.

In order to assess the efficiency of the correction proposed in Section 3, a simple Riemann problem was solved numerically. The left state was taken equal to -5 and the right state

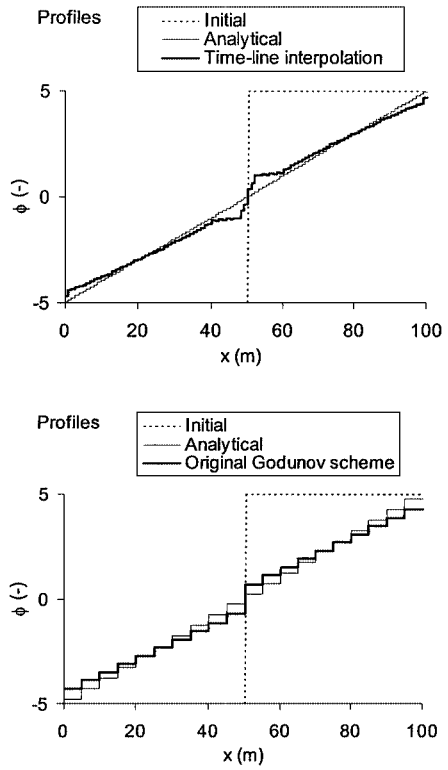

FIG. 5. Solution of the Riemann problem for the inviscid Burgers equation after 10 time steps with a maximum Courant number of 5 (top) and 1 (bottom). For Courant numbers smaller than or equal to unity, the original Godunov scheme is obtained.

was taken equal to $+5$ (arbitrary units). The analytical solution consists of a rarefaction wave spreading in both directions from the location of the initial discontinuity. The initial discontinuity ($x = 50$) then becomes a sonic point. The time step Δt was taken equal to 1, and two cell sizes were used: 1 and 5. The maximum Courant number in the domain is 5 for $\Delta x = 1$, while it is equal to 1 for $\Delta x = 5$. For Courant numbers smaller than or equal to unity, the scheme switches to the original, first-order Godunov scheme. Figure 5 shows the profiles obtained after 10 time steps using the linear time reconstruction with the correction at sonic points. The computed profile is observed to exhibit an artificial steepening about the sonic point, regardless of the value of the Courant number. This phenomenon, which is a well-known characteristic of the original Godunov scheme (viz. Figure 5, bottom), is caused by the low-order reconstruction of the flow variable in the cells that contain the sonic point or the neighboring cells. This is due to the wave speed and the flow variable ϕ being subject to large relative changes. In this case, the piecewise constant reconstruction of the Godunov scheme is not accurate enough to provide a correct estimate of the left and right states of the Riemann problem. Such a problem can be easily eliminated for Courant numbers smaller than unity by adopting a higher-order reconstruction, as in MUSCL or other higher-order schemes [16, 25, 27, 28, 30]. For Courant numbers larger than unity, the profile is not constant in space, but it is in time at the cell interface (because Eq. (24c) is applied). As shown by the present computational example, taking the time slope of the variable equal to zero around the sonic point yields a degradation in the quality of the computational solution.

Further improvements of the method should focus on a more accurate estimate of the slope s than is currently used in Eq. (24c).

In a way similar to the linear scalar case, the accuracy of the proposed method suffers from the propagation of the dissipation introduced by the slope limiter from one interface to the next via the recurrence relationships. Therefore, and for the same reasons as in the linear case, the proposed method does not have the same accuracy as the variable-stencil-based schemes proposed in [13–15, 18, 19]. The accuracy of the proposed scheme could be improved by using a more accurate procedure (see, e.g., [16]) to determine the times τ and τ' associated with the location of the arrival and departure points of the characteristics shown in Fig. 1, but this would be at the expense of computational rapidity.

5.3. Free Surface Flow Equations

The proposed schemes were applied to the shallow water equations in rectangular canals without bottom slope and bed friction, for which the vectors $\mathbf{U}$ and $\mathbf{F}$ in Eq. (1) assume the form

$$\mathbf{U} = (h, q)^T, \quad \mathbf{F} = \left(q, \frac{q^2}{h} + \frac{gh^2}{2} \right)^T, \tag{35}$$

where g is gravity, h is the water depth, and q denotes the discharge per unit width in the canal. An approximate-state solver was used to solve the Riemann problems at the cell interfaces [28]. Dambreak problems were solved, i.e., Riemann problems where water is initially at rest. Two configurations were tested. Their characteristics are summarized in Table I.

These classical problems give rise to a rarefaction wave traveling to the left and to a shock traveling to the right. In the first problem, the flow never becomes supercritical, whereas in problem 2, a critical point appears at the location of the initial discontinuity.

Figure 6 shows the solution obtained for problem 1. Both constant and linear time reconstructions were used. The cell size Δx was taken equal to 1 m. The time step was equal to $\Delta t = 0.2$ s. The maximum Courant number over the domain was found to be equal to 5.76 whereas its minimum value was 0.89. Both computations and the analytical solution are displayed for $t = 5$ s. The figure shows that the linear time reconstruction brings a significant improvement over the constant time reconstruction. The constant reconstruction needs twice as many cells to represent the shock wave as does the linear one.

Figure 7 shows the solution obtained for problem 2. Both constant and linear time reconstructions were used. The cell size Δx was taken equal to 1 m, but since the wave speeds involved in this test were higher than in problem 1, the time step was reduced to $\Delta t = 0.1$ s. The maximum Courant number over the domain was found to be equal to 6.75, while its minimum value was 0.82. Both computations and the analytical solution are displayed for $t = 5$ s.

TABLE I
Characteristics of the Riemann Problems

Problem	h_L (m)	h_R (m)	q_L (m · s^{-1})	q_R (m · s^{-1})
1	50	30	0	0
2	50	5	0	0

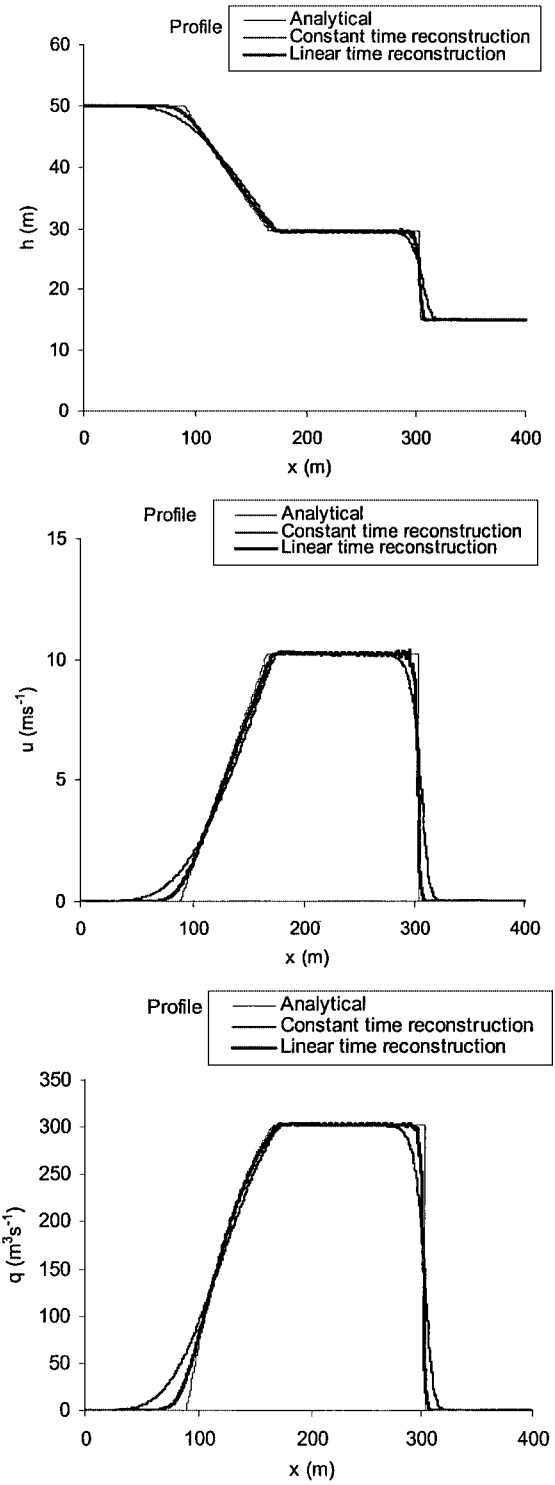

FIG. 6. Solution of the first dam-break problem for a maximum Courant number of 5.5: water depths (top), velocities (middle), and discharges (bottom) at $t = 5$ s.

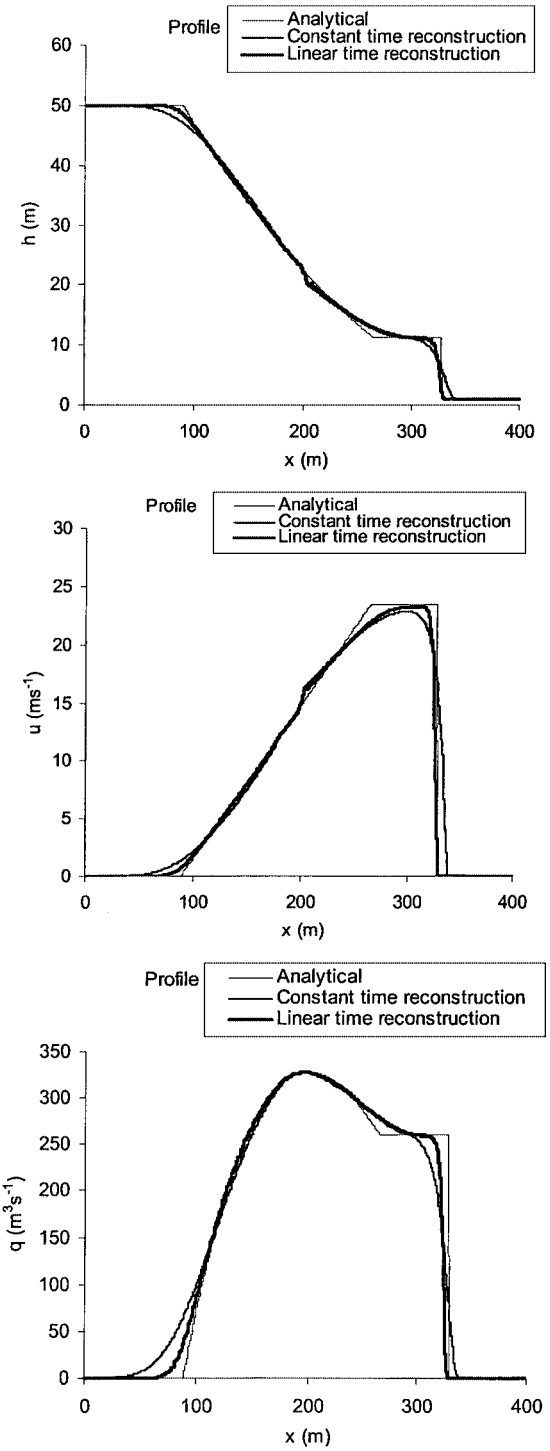

FIG. 7. Solution of the second dam-break problem for a maximum Courant number of 6.75: water depths (top), velocities (middle), and discharges (bottom) at $t = 5$ s.

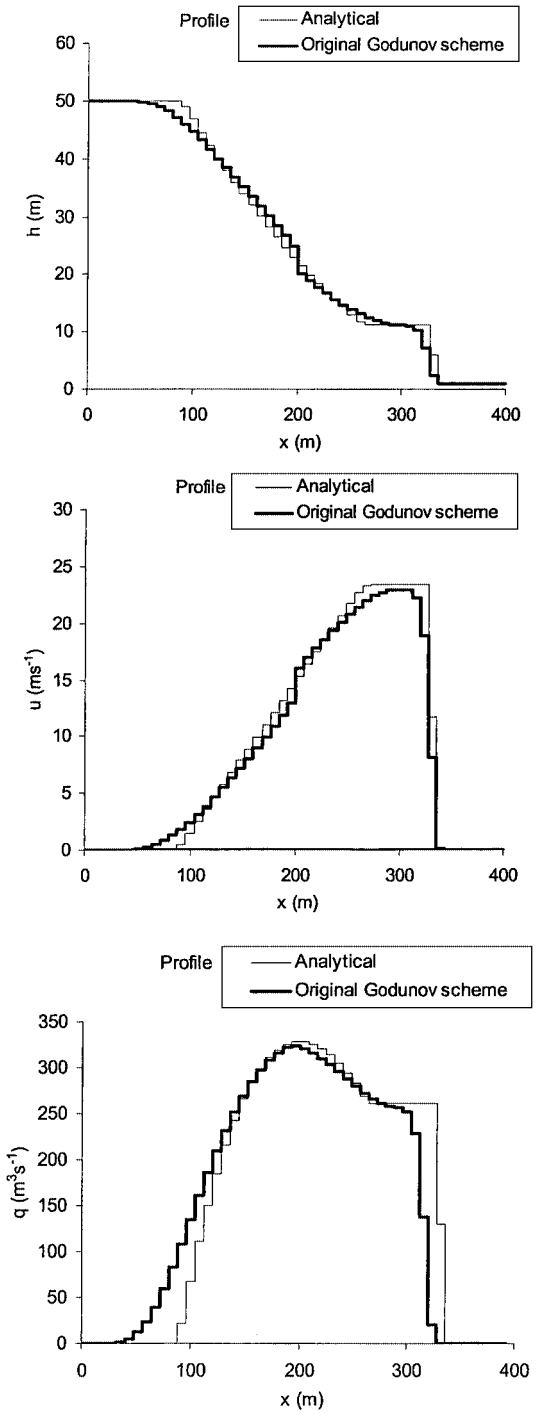

FIG. 8. Solution of the second dam-break problem using the original Godunov scheme with a maximum Courant number of 0.84: water depths (top), velocities (middle), and discharges (bottom) at $t = 5$ s.

The figure shows that although the computed profiles are smoother than the analytical one, the amplitude and the speed of the shock are correctly computed. The computed water depth and velocity exhibit an artificial steepening about the location of the initial discontinuity. As is observed in the case of the inviscid Burgers equation, this is a characteristic behavior of the solution obtained by the original Godunov scheme for Courant numbers smaller than unity when a low-order reconstruction is used around the critical point.

Indeed, the original, first-order Godunov scheme applied to the dam-break problem also exhibits an artificial steepening of the profile at the supercritical point, even though the Courant number is smaller than unity. The low-order reconstruction of the first-order scheme yields an underestimation of the momentum flux at the critical point. This results in a smaller discharge in the numerical solution than in the analytical one. Consequently, water is being retained artificially upstream of the supercritical point, whereas there is a deficit of mass downstream, and the profile is steeper in the numerical solution than in the analytical one. This problem of flux underestimation can be eliminated using a higher-order reconstruction, as shown by comparisons made in the past between various schemes of increasing accuracy [16]. The present problem proceeds from the same mechanism of flux underestimation, but it is amplified when a large time step is adopted in the simulation (note however that no instability occurred in the solution, even without the critical point correction). The proposed correction can be seen as a higher-order modification of both the location of the foot of the characteristic and the reconstruction in time. This is confirmed by Fig. 8, which shows the computed profile using the same initial conditions and simulation time step, but with a cell size $\Delta x = 8$ m instead of 1 m. Then, the maximum Courant number within the computational domain is equal to 0.84 instead of 6.75 and the method switches to the original, first-order Godunov scheme. The artificial steepening of the computed depth and velocity profiles can be observed in this simulation too. This problem can be avoided in a way similar to the Burgers equation for Courant numbers smaller than unity using a higher-order reconstruction of the profile within the computational cell. For Courant numbers larger than unity, a better estimate than Eq. (24c) should be proposed for the estimate of the slope s around critical points. Still, it is surprising to notice that the size and amplitude of the steep region remains almost constant for all values of Δx.

6. CONCLUSIONS

Two unconditionally stable, Godunov-type schemes have been presented for the solution of hyperbolic systems of conservation laws. The equivalence between space and time for the solutions of hyperbolic systems is used to extend the domain of dependence of the solution in time rather than in space. Two schemes are proposed: the first one is based on a constant reconstruction of the flow variables over time; the second one uses a linear reconstruction and incorporates a slope limiter. Similarly to the classical reconstruction over space, the reconstruction of the flow variables over time plays a decisive role in the accuracy of the scheme. When no limiter is incorporated into the linear reconstruction version, the amplification factor of the scheme is equal to unity for all Courant numbers larger than unity and for all wave numbers. A specific treatment is proposed for critical points. The proposed schemes were tested on the scalar advection equation, the inviscid Burgers equation, and the 2×2 system of PDEs that describe shallow water flow. Dam-break simulations showed the superiority of the linear time reconstruction over the constant one. Owing to the

strong numerical diffusion introduced by the limiters, the proposed schemes cannot be used in all circumstances, and in particular not when both sonic waves and strong shocks are present in the solution. However, for many problems in the field of river or pipe hydrodynamics and contaminant transport, the proposed schemes appear as a viable alternative to a number of (more diffusive) classical implicit schemes. They can be used to solve hyperbolic systems of conservation laws with high contrasts between the various wave speeds or in the cell sizes. They are also seen as good candidates for steady state simulations. Another possible application of these schemes may consist of providing reasonably converged solutions within the iteration loops of implicit schemes, which would allow computational time to be saved.

APPENDIX A

Recurrence Relationships for the Linear Time-Line Reconstruction

The profile is sought in the form

$$\phi_{j-1/2}(t) = \bar{\phi}_{j-1/2} + \left(t - t^n - \frac{\Delta t}{2}\right) s_{j-1/2}. \tag{A1}$$

This is illustrated in Fig. A1a. From interface $j - 1/2$ to interface $j + 1/2$, this profile is translated by an amount $(\tau - t^n)$. Therefore, at the interface $j + 1/2$, the expression of ϕ becomes

$$\phi(t) = \phi_j^n \quad \text{for } t \le \tau, \tag{A2a}$$

$$\phi(t) = \bar{\phi}_{j-1/2} + \left(t - \tau - \frac{\Delta t}{2}\right) s_{j-1/2} \quad \text{for } t > \tau. \tag{A2b}$$

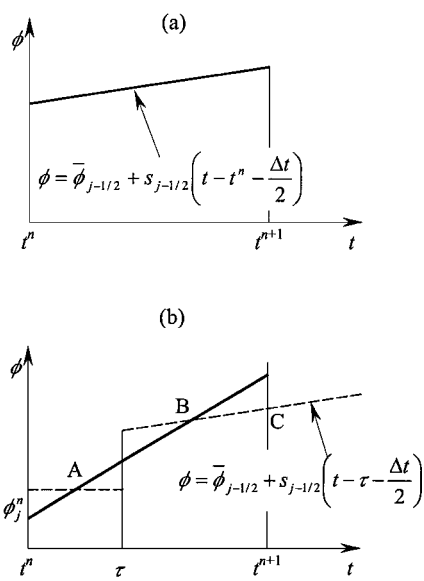

FIG. A1. Linear time-line interpolation (a) at the interface $j - 1/2$ and (b) at the interface $j + 1/2$. From (a) to (b) the linear profile is shifted by $(\tau - t^n)$ (right-hand side, dashed line on (b)) and the average between times 0 and t is equal to ϕ_j^n (left-hand side, dashed line on (b)). From these two piecewise linear profiles, a new continuous, linear profile is defined (thick line on (b)).

The integral between 0 and Δt of the equivalent linear reconstruction over time,

$$\phi_{j+1/2}(t) = \bar{\phi}_{j+1/2} + \left(t - t^n - \frac{\Delta t}{2}\right) s_{j+1/2}, \tag{A3}$$

has to be the same as the integral of the piecewise linear profile defined by Eqs. (A2). This condition leads to the following expression for $\bar{\phi}_{j+1/2}$:

$$\bar{\phi}_{j+1/2} = \frac{\phi_j^n}{Cr} + \left(1 - \frac{1}{Cr}\right)\left(\bar{\phi}_{j-1/2} - \frac{\Delta t}{2Cr} s_{j-1/2}\right), \tag{A4a}$$

$$Cr = \frac{\Delta t}{\tau - t^n}. \tag{A4b}$$

But it can be checked that any value of the slope $s_{j+1/2}$ would satisfy the equality of the integrals. It was decided to use the average slope between the two piecewise linear profiles defined by Eqs. (A2). This is the slope of the straight line (AC) in Fig. A1. This slope is given by

$$s_{j+1/2} = -\frac{2}{\Delta t}\phi_j^n + \frac{2}{\Delta t}\bar{\phi}_{j-1/2} - \frac{1}{Cr} s_{j-1/2}. \tag{A5}$$

Since this reconstruction is likely to induce overshooting in the solution, the slope is limited in such a way that the minimum and maximum of the profile given by (A3) are always constrained between those of the piecewise linear profile defined by Eqs. (A2). To do so, the following intermediate slopes are computed.

$$\sigma_1 = 2\frac{\bar{\phi}_{j+1/2} - \phi_j^n}{\Delta t}, \tag{A6a}$$

$$\sigma_2 = 2\frac{\bar{\phi}_{j-1/2} + \Delta t\left(\frac{1}{2} - \frac{1}{2Cr}\right) s_{j-1/2} - \bar{\phi}_{j+1/2}}{\Delta t}, \tag{A6b}$$

where σ_1 represents the slope between points D and E on Fig. A1 and σ_2 represents the slope between points E and F (see Fig. A1). The limiter functions in the classical manner were introduced [30] for linear reconstructions with respect to space. $S_{j+1/2}$ is corrected as follows:

$$s_{j+1/2} = \sigma_1 \quad \text{if } \sigma_1 s_{j+1/2} \geq 0 \text{ and } |\sigma_1| < s_{j+1/2}, \tag{A7a}$$

$$s_{j+1/2} = \sigma_2 \quad \text{if } \sigma_2 s_{j+1/2} \geq 0 \text{ and } |\sigma_2| < s_{j+1/2}, \tag{A7b}$$

$$s_{j+1/2} = 0 \quad \text{if } \sigma_1\sigma_2 \leq 0. \tag{A7c}$$

This guarantees the TVD character of the scheme and allows spurious oscillations to be eliminated.

APPENDIX B

Linear Stability Analysis for the Linear Time Reconstruction

The solution is sought in the form

$$\bar{\phi}_{j+1/2} = \phi_{1/2}^{1/2} \exp(\lambda n\Delta t + \mu j\Delta x), \tag{B1a}$$

$$s_{j+1/2} = s_{1/2}^{1/2} \exp(\lambda n\Delta t + \mu j\Delta x), \tag{B1b}$$

$$\phi_j^n = \phi_0^0 \exp(\lambda n\Delta t + \mu j\Delta x), \tag{B1c}$$

with

$$\lambda = \lambda_r + i\lambda_i, \tag{B2a}$$

$$\mu = i\mu_i, \tag{B2b}$$

$$i^2 = -1. \tag{B2c}$$

Substituting Eqs. (B1) into Eqs. (25), (A4a), and (A5) and dividing by $\phi_{1/2}^{1/2}$ yields the relationships

$$\exp(i\mu_i \Delta x) = a\varepsilon + b + c\eta, \tag{B3a}$$

$$\exp(i\mu_i \Delta x)\eta = d\varepsilon + e + f\eta, \tag{B3b}$$

$$\varepsilon \exp(\lambda \Delta t) = (1 - ga)\varepsilon + g(1 - b) - gc\eta, \tag{B3c}$$

where $\varepsilon = \phi_1^0/\phi_{1/2}^{1/2}$ and $\eta = s_{1/2}^{1/2}/\phi_{1/2}^{1/2}$. Solving Eqs. (B3a) and (B3b) for ε and η yields

$$\varepsilon = \frac{(2 - Cr)\exp(i\mu_i x) + Cr\exp(2i\mu_i x)}{[1 + \exp(i\mu_i \Delta x)]}, \tag{B4a}$$

$$\eta = 2\frac{Cr[1 - \exp(i\mu_i \Delta x)]}{\Delta t[1 + \exp(i\mu_i \Delta x)]}. \tag{B4b}$$

The amplification factor $A_n = \frac{\phi_j^{n+1}}{\phi_j^n} = \exp(\lambda \Delta t)$ is obtained by introducing Eqs. (B4) into Eq. (B3c) and solving for A_n:

$$A_n = \frac{2 + Cr[\exp(-i\mu_i \Delta x) - 1]}{2 + Cr[\exp(i\mu_i \Delta x) - 1]}. \tag{B5}$$

In Eq. (B5), the numerator is equal to the conjugate of the denominator and therefore $|A_n| = 1$. The global amplification factor is given by

$$Ag = A_n^{1/Cr} \tag{B6}$$

and is also equal to unity. The phase convergence factor C_n is given by

$$C_n = -\frac{\lambda_i}{\mu_i} = -\frac{Arg(A_n)}{2\pi}\frac{M}{Cr}. \tag{B7}$$

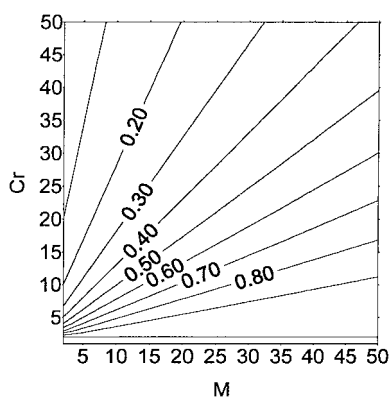

FIG. B1. Phase convergence factor for the linear time reconstruction.

Figure B1 shows the variations of C_n as a function of M and Cr. Note that for $Cr = 2$, Eq. (B5) can be simplified to

$$A_n = \exp(-2i\mu_i x) \tag{B8}$$

and, therefore, $C_n = 1$ and the analytical solution is obtained.

ACKNOWLEDGMENT

The author would like to thank Professor Rosinger from the University of Pretoria, South Africa, for the fruitful discussions and exchange of ideas on stability issues.

REFERENCES

1. P. R. Woodward and P. Colella, The simulation of two-dimensional fluid flow with strong shocks, *J. Comput. Phys.* **54**, 115 (1984).
2. E. F. Toro, *Riemann Solvers and Numerical Methods for Fluid Dynamics* (Springer-Verlag, Berlin Heidelberg, 1997).
3. S. C. Chang, The method of space-time conservation element and solution element—a new approach for solving the Navier–Stokes and Euler equations, *J. Comput. Phys.* **119**, 295 (1995).
4. S. C. Chang, X. Y. Wang, and C. Y. Chow, The space-time conservation element and solution element method: a new high-resolution and genuinely multidimensional paradigm for solving conservation laws, *J. Comput. Phys.* **156**, 89 (1999).
5. J. Greesier and J.-M. Moschetta, *On the Pathological Behavior of Upwind Schemes*, AIAA Paper 98-0110 (1998).
6. E. E. Rosinger, *Nonlinear Equivalence, Reduction of PDEs to ODEs and Fast Convergent numerical methods* (Pitman, Boston, 1982).
7. E. E. Rosinger, Propagation of round-off errors and the role of stability in numerical methods for linear and nonlinear PDEs, *Appl. Math. Modelling* **9**, 331 (1985).
8. E. E. Rosinger, Convergence paradox in numerical methods for linear and nonlinear PDEs, in *Advances in Computer Methods for PDEs*, edited by R. Vitchnevetski and R. S. Steepleman (IMACS, NJ, 1987), Vol. 6, p. 431.
9. E. E. Rosinger, Optimal accuracy of unconditionally stable explicit method for non linear evolution PDEs, *Applied Math. Lett.* **7**(5), 97 (1994).
10. D. E. Goldberg and B. Wylie, Characteristic method using time-line interpolations, *J. Hydraul. Eng. (ASCE)* **109**(5), 670 (1983).
11. A. Staniforth and J. Côté, Semi-Lagrangian integration schemes for atmospheric models: a review, *Mon. Weather Rev.* **119**, 1335 (1999).
12. B. P. Leonard, Note on the von Neumann stability of explicit one-dimensional advection schemes, *Comp. Methods Appl. Mech. Eng.* **118**, 29 (1994).
13. B. P. Leonard, A. P. Lock, and M. K. McVean, The NIRVANA scheme applied to one-dimensional advection, *Int. J. Numer. Methods Heat Fluid Flow* **5**, 341 (1995).
14. B. P. Leonard, A. P. Lock, and M. K. McVean, Conservative explicit unrestricted-time-step multidimensional constancy-preserving advection schemes, *Mon. Weather Rev.* **124**, 2588 (1996).
15. P. J. Roache, A flux-based modified method of characteristics, *Int. J. Numer. Methods Fluids* **15**, 1259 (1992).
16. S. Savic and F. M. Holly, Jr., Dambreak flood waves computed by modified Godunov method, *J. Hydraul. Res.* **31**, 187 (1993).
17. A. McDonald, An examination of alternative extrapolations to find the departure point in a 'two-time-level' semi-Lagrangian integration. *Mon. Weather Rev.* **127**, 1985 (1999).

18. R. J. LeVeque, Large time step shock-capturing techniques for scalar conservation laws, *SIAM J. Numer. Anal.* **19**(6), 1091 (1982).
19. R. J. LeVeque, Convergence of a large time step generalization of Godunov's method for conservation laws, *Commun. Pure Appl. Math.* **37**, 463 (1984).
20. R. J. LeVeque, High resolution finite volume methods on arbitrary grids via wave propagation, *J. Comput. Phys.* **78**, 36 (1988).
21. B. A. Fryxell, P. R. Woodward, P. Colella, and K. H. Winckler, An implicit-explicit hybrid method for Lagrangian hydrodynamics, *J. Comput. Phys.* **63**, 283 (1986).
22. J. P. Collins, P. Colella, and H. M. Glaz, An implicit-explicit Eulerian Godunov scheme for compressible flow, *J. Comput. Phys.* **116**, 195 (1995).
23. W. Dai and P. R. Woodward, Iterative implementation of an implicit-explicit hybrid scheme for hydrodynamics, *J. Comput. Phys.* **124**(1), 217 (1996).
24. W. Dai and P. R. Woodward, A second-order iterative implicit-explicit hybrid scheme for systems of conservation laws, *J. Comput. Phys.* **128**(1), 181 (1996).
25. M. Ben-Artzi and J. A. Falcovitz, second-order Godunov-type scheme for compressible fluid dynamics, *J. Comput. Phys.* **55**, 1 (1984).
26. M. Ben-Artzi and J. Falcovitz, Application of the generalised Riemann problem method to 1-D compressible flow with interfaces, *J. Comput. Phys.* **65**, 170 (1986).
27. P. Colella and P. R. Woodward, The piecewise parabolic method (PPM) for gas-dynamical simulations, *J. Comput. Phys.* **54**, 174 (1984).
28. V. Guinot, The discontinuous profile method (DPM) for simulating two-phase flow in pipes using the single-component approximation, *Int. J. Numer. Methods Fluids* **38**, 567 (2002).
29. G. B. Whitam, *Linear and Non-Linear Waves* (Wiley, New York, 1974).
30. B. Van Leer, Toward the ultimate conservative difference scheme. V. A second-order sequel to Godunov's method, *J. Comput. Phys.* **32**, 101 (1979).